7-21-2008

Terahertz photomixing spectroscopy of two-dimensional semiconductor plasmons

Todd Barrick

TERAHERTZ PHOTOMIXING SPECTROSCOPY OF TWO-DIMENSIONAL SEMICONDUCTOR PLASMONS

BY

TODD A. BARRICK

B.S., ELECTRICAL ENGINEERING
UNIVERSITY OF NEW MEXICO,
2006

THESIS

Submitted in Partial Fulfillment of the
Requirements for the Degree of

Masters of Science,
Electrical Engineering

The University of New Mexico
Albuquerque, New Mexico

May, 2008

Dedication

To my mom and dad, my sisters April and Jenny, and my brothers Steve and John for holding me up and pushing me forward. Your unconditional love and support made every day worthwhile and helped me to achieve my goals.

To my close friends Sean, Sam, and Ruth for always being there for me.

To my friend and mentor Dr. Scott Crooker, for the wealth of skills you have taught me, keeping me on course, and always pushing me to succeed.

Acknowledgments

I would like to express my deepest gratitude to my good friend and research advisor Dr. Eric Shaner for his patience, guidance, comic relief, many late hours, and faith throughout this research.

To Dr. Kevin Fortier for working along with me and always taking the time to help me out, for his valuable suggestions and advice, without whom I couldn't have made it.

To Dr. Michael Wanke for taking a chance on me, helping me to succeed, and teaching me a wealth of knowledge.

To Dr. Igal Brener for the valuable skills he has taught me in the lab and his patience and guidance through this experience.

I would like to thank my advisor Dr. Charles Fleddermann for his help in making this experience possible and for his advice and support.

I would also like to thank Dr. Chaouki Abdallah for his valuable recommendations and guidance throughout my education.

To my good friends Jeremy Wright and Karl Westlake who helped to make this research possible and for all the valuable comments and suggestions throughout this experience.

To Chuck, Albert, Xomalin, and all the members of the THz Team for all the help they have given me throughout my research.

And to all my friends and family who make every day worthwhile.

TERAHERTZ PHOTOMIXING SPECTROSCOPY OF TWO-DIMENSIONAL SEMICONDUTOR PLASMONS

BY

TODD A. BARRICK

ABSTRACT OF THESIS

Submitted in Partial Fulfillment of the
Requirements for the Degree of

Masters of Science,
Electrical Engineering

The University of New Mexico
Albuquerque, New Mexico

May, 2008

TERAHERTZ PHOTOMIXING SPECTROSCOPY OF TWO-DIMENSIONAL PLASMONS

By

Todd A. Barrick

B.S., Electrical Engineering, University of New Mexico, 2006
M.S., Electrical Engineering, University of New Mexico, 2008

ABSTRACT

This thesis reports the findings of terahertz photomixer spectroscopy performed on plasmonic grating-gate detectors made from high mobility two-dimensional electron gas (2DEG) material. In recent years, these detectors have seen significant improvements in sensitivity and currently exhibit a noise equivalent power of $10^{-8} W/\sqrt{Hz}$. However, further improvements are essential for these detectors to become truly useful; the ultimate goal being a NEP $<10^{-10} W/\sqrt{Hz}$. To this end, it is necessary to understand the physical properties of the mechanism underlying the detectors photoresponse, namely plasmons. Although two-dimensional plasmons were first observed in semiconductors in 1978, to date, their physical properties, for example scattering and absorption cross section, are relatively unknown. The primary purpose of this work is to develop a measurement system capable of revealing these properties and utilize this system to understand the absorption of radiation by two-dimensional plasmons. By no means will the study of plasmonic properties using this system end when this work is completed. Rather, this work lays the foundation for years of future research in this field.

Contents

List of Figures

List of Tables

Chapter 1

Terahertz Photomixing Spectroscopy

1.1 Introduction

Recently there has been an increased interest in the terahertz regime of the electromagnetic spectrum. It has been found that terahertz (THz) radiation allows observation of the spectral fingerprints of gases, spectroscopy of material compositions, and unique imaging capabilities. This has allowed significant advances in the potential for homeland security measures as well as aiding in the progression of the fundamental sciences.

Various techniques for THz generation have allowed researchers to explore the applications of this growing field. THz sources such as quantum cascade lasers, black-bodies, free-electron lasers, and time-domain spectroscopy systems are commonly explored in many labs. As with any modern day THz source, these all have advantages and drawbacks. For this work, the THz source of choice is a photomixer system based on photoconductive antennas. In this thesis the theory behind photomixing spectroscopy will be explored and the design of the spiral antennas used for THz generation will be

reviewed. Then the design and setup of the photomixing system used for the exploration of two-dimensional surface plasmons will be discussed.

1.2 Theory

Terahertz Photomixing Spectroscopy evolved from a desire to have a high resolution tunable spectrometer that performed at sub-mm wavelengths. At these wavelengths chemical identification can be performed where other portions of the spectrum do not see distinction. This can be attributed to rotational and vibrational resonances in molecules; essentially, in the THz, one can gain information about not just atomic composition, but also the arrangement of atoms. Therefore, by taking high resolution spectra at these frequencies, one can identify spectral fingerprints of chemicals that are not possible using other spectroscopic techniques. This has shown a great deal of promise in the field of homeland security where there is a need for an unobtrusive means of chemical detection at airports or train stations, for example.

Photomixing relies on the concept of mixing two coherent high frequency sources onto a photoconductive emitter (**Figure 1-1**). The electromagnetic wave output of the photoconductive emitter (antenna) is dependant on the difference frequency (beat frequency) of the two coherent sources. This high resistivity emitter is engineered to have electron-hole pair recombination times on the order of a picosecond. Electrodes to induce an electric field are then deposited on the surface of the low carrier lifetime material. For the purpose of this thesis ErAs:GaAs photomixing antennas were used. When illuminated, the incident photons (which exceed the bandgap energy of GaAs) generate electron-hole pairs within the emitter. The induced electric field generated by

DC bias of the electrodes gives rise to a drift current of excess carriers within the material. It is the modulated temporal profile of these excess carriers generated by the photomixed beam on the electrodes of the antenna that creates THz radiation.

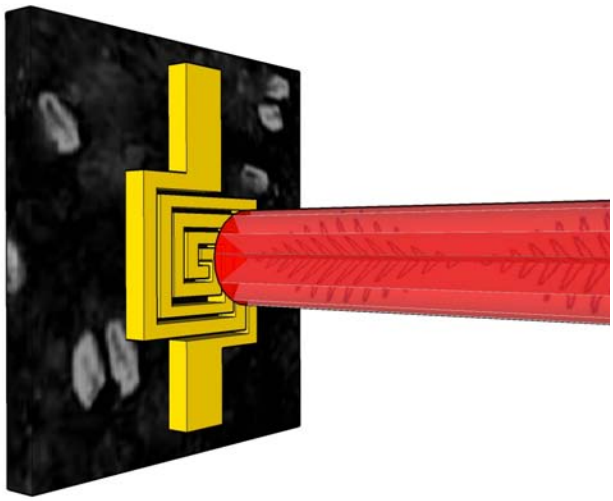

Figure 1-1: Photomixed beam incident on a spiral photoconductive emitter

Consider two electric fields

$$\mathbf{E_1} = E_0 \cos(\omega_1 t) \tag{1.1}$$

$$\mathbf{E_2} = E_0 \cos(\omega_2 t) \tag{1.2}$$

of same amplitude E_0 and differing frequencies ω_1 and ω_2. The sum of these two waves generates an amplitude modulated wave of carrier frequency

$$\omega_p = \frac{(\omega_1 + \omega_2)}{2} \tag{1.3}$$

and envelope frequency

$$\omega_g = \frac{|\omega_1 - \omega_2|}{2} \tag{1.4}$$

the sum of these two waves is given by

$$\mathbf{E_T} = 2E_0 \cos(\omega_p t)\cos(\omega_g t) \tag{1.5}$$

where the first term describes the high frequency component of the amplitude modulated wave and the second term describes the envelope frequency, [15].

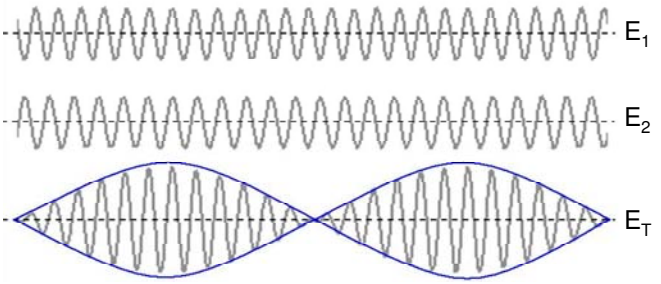

Figure 1-2: The sum of two waves of different frequencies. The sum of these waves generates a wave whose frequency is equal to the difference in frequency between the original waves.

This type of wave disturbance exhibits a phenomenon known as a beat frequency. As shown in **Figure 1-2** the sum of two waves creates pulses modulated at twice the envelope frequency

$$\omega_{beat} = 2\omega_g = 2\left(\frac{|\omega_1 - \omega_2|}{2}\right) = |\omega_1 - \omega_2| \tag{1.6}$$

The term 'beat frequency' comes from the beating sound that is generated when two sound waves of differing frequency are added together. Converting from radial frequency, (1.6) is reduced to

$$f_{beat} = |f_1 - f_2| \tag{1.7}$$

We see from (1.7) that the beat frequency is simply given by the difference in frequency between the two electric fields.

As was described before, the electromagnetic wave output of the photoconductive antenna is dependant on the difference or beat frequency of the incident beams defined by (1.7). Incident photons (with energy greater than the bandgap energy of GaAs) generate electron-hole pairs within the substrate of the GaAs material. Biasing the electrodes on

the surface of the substrate generates an electric field which produces a drift current in the GaAs (**Figure 1-3**). This drift current (or photocurrent) is modulated at the beat

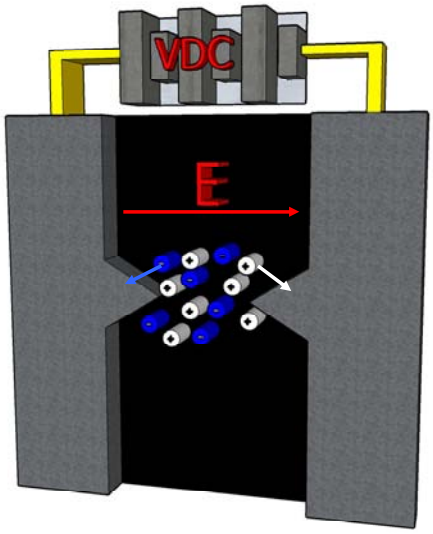

Figure 1-3: Charge separation in an antenna from the applied DC electric field.

frequency of the incident electromagnetic wave. This process is governed by the differential equations

$$\begin{aligned} \frac{dn}{dt} &= G_e(t) - R_e \quad \text{(electrons)} \\ \frac{dp}{dt} &= G_h(t) - R_h \quad \text{(holes)} \end{aligned} \tag{1.8}$$

The generation rate, G, derived from the Poynting Vector is given by

$$G = \alpha \frac{P_{opt}}{\hbar \omega_p} \tag{1.10}$$

where α is the absorption coefficient, ω_p is the carrier frequency of the mixed beam, and

$$P_{opt} = \left(E_1 + E_2\right)^2 \tag{1.11}$$

is the incident optical power. Expanding (1.11), the optical power becomes

$$P_{opt} = E_0^2 \cos^2(\omega_1 t) + E_0^2 \cos^2(\omega_2 t) + E_0^2 \left[\cos((\omega_1 - \omega_2)t) + \cos((\omega_1 + \omega_2)t)\right]$$
$$P_{opt} = \underbrace{E_0^2 \cos^2(\omega_1 t) + E_0^2 \cos^2(\omega_2 t)}_{(a)} + \underbrace{E_0^2 \left[\cos(\omega_{beat} t) + \cos((\omega_1 + \omega_2)t)\right]}_{(b)} \quad (1.12)$$

where (a) is the contribution from the individual waves and (b) is created from the mixing of the two waves. For simplification we will concentrate only on the part of the expression that is dependant on the beat frequency, reducing (1.12) to

$$P_{opt} = E_0^2 \cos(\omega_{beat} t) \quad (1.13)$$

The generation rate then becomes

$$G = G_0 \cos(\omega_{beat} t)$$

where

$$G_0 = \alpha \frac{E_0^2}{\hbar \omega_p}$$

The recombination rate, *R*, is given by

$$R = \frac{n}{\tau} \quad \text{(for electrons)} \quad (1.14)$$

where *n* is the carrier density and τ is the recombination time. For electrons this gives

$$\frac{dn}{dt} = G_0 \cos(\omega_{beat} t) - \frac{n}{\tau}$$

A similar expression is given for holes. The solution to this differential equation is then

$$n(t) = \tau G_0 \frac{\left[\omega_{beat} \tau \sin(\omega_{beat} t) + \cos(\omega_{beat} t)\right]}{\omega_{beat}^2 \tau^2 + 1} + C e^{\frac{-t}{\tau}} \quad (1.15)$$

where *C* is a constant derived from initial conditions. Shown in **Figure 1-4** is a plot of the carrier density for three different recombination lifetimes. From this graph we can see from this plot that as the carrier recombination time increases the oscillatory term in

the carrier density dies out. This shows that in order to have THz emission the recombination time must be shorter than $1/\omega_{beat}$, therefore $\tau \approx 1ps$. These ultra short lifetimes are characteristic of such materials as low-temperature grown GaAs and embedding GaAs with recombination centers such as ErAs. Therefore because of this

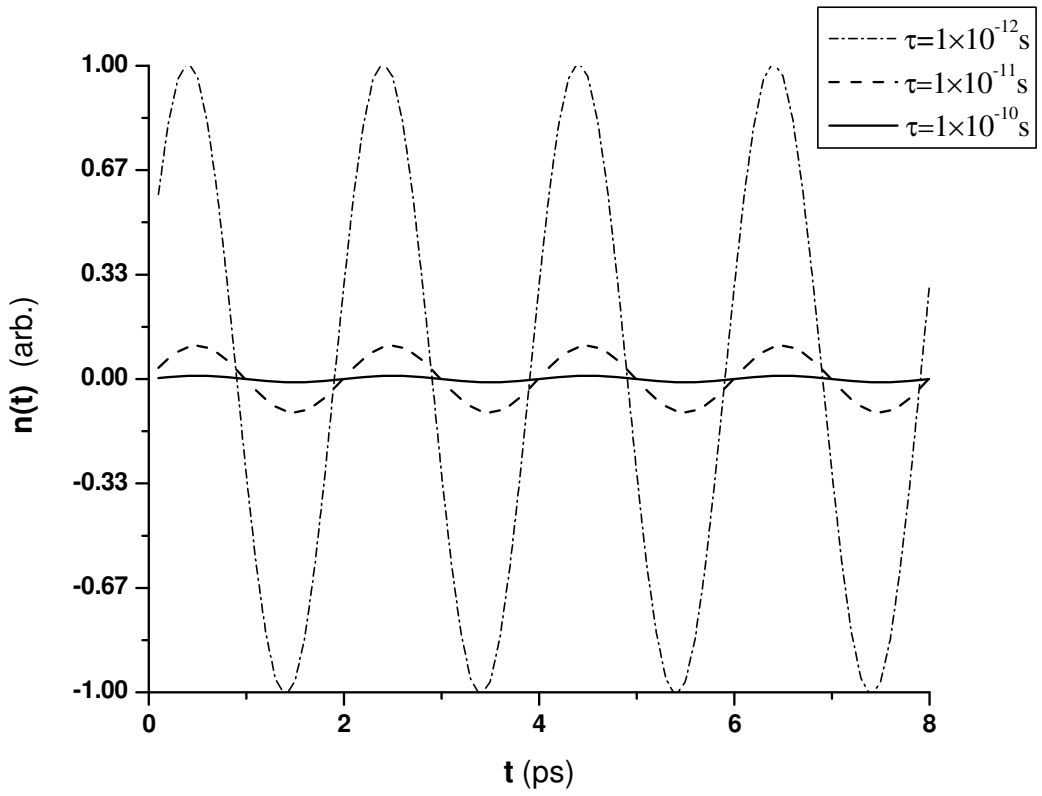

Figure 1-4: Plot of Carrier Density for three different carrier lifetimes as a function of frequency. This plot shows that as the recombination time (τ) increases, the amplitude of the oscillatory part of the carrier density (n(t)) decreases.

design constraint and the high frequencies of ω_1 and ω_2 it was valid to ignore the other oscillating terms in (1.12).

1.3 Experimental Setup

The THz photomixing system described in this thesis was designed to characterize plasmon resonance in grating-gate THz detectors. Shown in **Figure 1-5** is a schematic diagram of the photomixing system used in these experiments. Two 100mW 780nm, tunable Littmann / Metcalf external cavity diode lasers purchased from Sacher Lasertechnik Group were used to generate the beat frequency. Laser 1 was locked to the Doppler broadened hyperfine structures in a Rb vapor cell as is diagramed in **Figure 1-6**. The hyperfine structures in Rb have a FWHM linewidth of ~6MHz . Side locking to a hyperfine structure provided stability stable within ~1MHz of $\lambda = 780.246nm$. The wavelength of laser 2 was monitored with a wavelength monitor that was accurate to $0.01nm$. This assured that the difference frequency between the two lasers was accurate when tuning the system to a specified frequency. Laser 2 was coarsely tuned by means

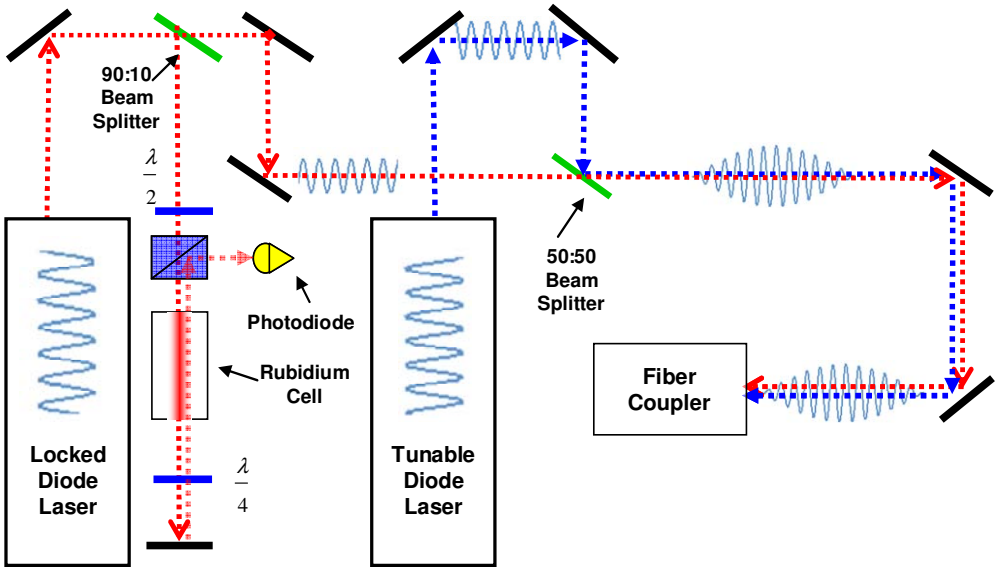

Figure 1-5: Diagram of the system where the two diode lasers are overlapped and coupled into a single mode fiber. Coupling into a single mode fiber guarantees that the two beams are spatially overlapped before hitting the photoconductive emitter. Part 1 of the setup.

of a serial connection to a built in controller that changed the angular position of a grating on an electromechanical actuator. This provided up to 100GHz modehop free tuning range at 780nm as specified by the manufacturer. These laser systems do provide an option to finely tune the laser using an integrated piezo-electric stack with up to 50MHz resolution, but this option was not used because fine tuning was not needed for these particular experiments. The lasers were combined on a 780nm AR coated 50:50 beam splitter by pairs of dielectric mirrors. The joined laser beams were then focused onto a 780nm single mode fiber to assure that they were overlapped. This was verified by monitoring the contributed laser power of each on a photodiode power meter. By measuring the laser power in the fiber it was shown that there is a maximum ~ 30% coupling efficiency into the fiber at 780nm, thus allowing a coupling of ~32mW of laser power.

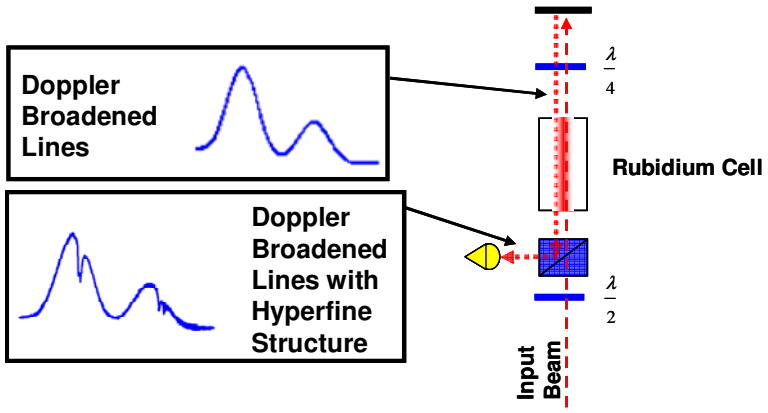

Figure 1-6: Setup for saturated absorption spectroscopy of Rb used diode laser locking. Locking to a hyperfine structure in Rb provides laser stability to ~1MHz.

The THz photomixing system was constructed in a two part system. Both parts of the system were contained within a nitrogen purge box. The first part contained the photomixing optics to combine and monitor the two lasers. The second part was fiber coupled to the first part and contained the THz spectroscopy system (**Figure 1-7**).

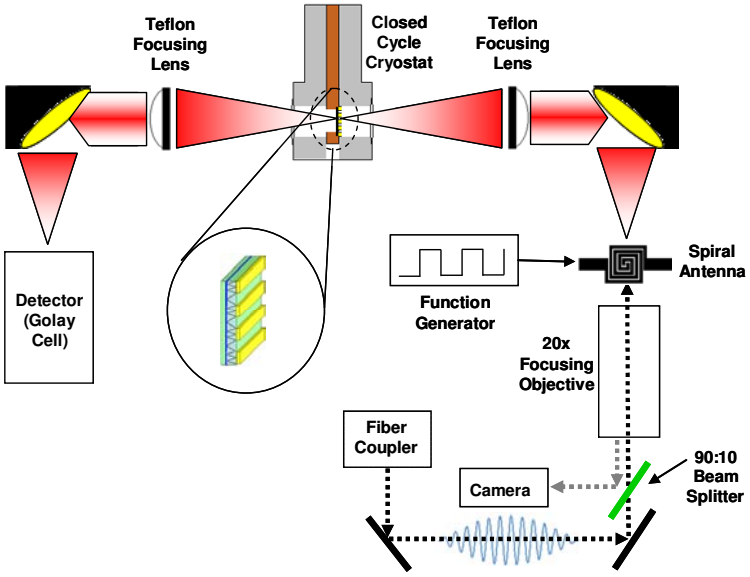

Figure 1-7: System for THz spectroscopy. The overlapped beams are mixed in the photoconductive antenna to generate THz radiation. The THz radiation is passed through the sample mounted in a closed cycle cryostat and detected by a Golay cell. Part 2 of the setup.

The output of the fiber coupler was directed into a 20x Mitutoyo focusing objective that focused the combined beams onto the ErAs:GaAs photomixing antenna (**Figure 1-8**).

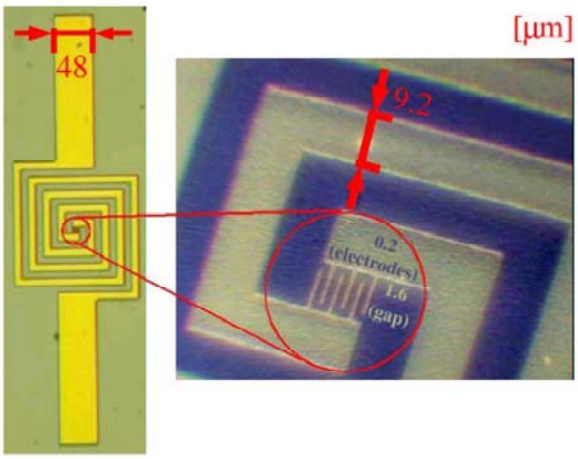

Figure 1-8: Picture showing the structure of the photomixing antenna. The close up image shows the small gap interdigitated fingers that provide the large bandwidth tuning range of the photomixing system. Figure taken from [3]

The THz emission from the switch was coupled to free space through a hyperhemispherical silicon lens. The radiation pattern from a photoconductive antenna

by itself is highly divergent. The silicon lens reduces the divergence and aids coupling into free-space (**Figure 1-9**). The THz emission was then collected and collimated in a

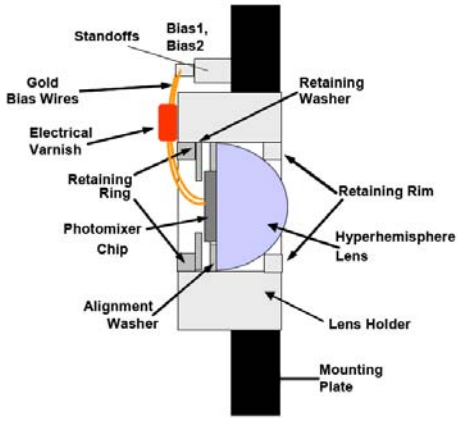

Figure 1-9: Diagram showing the construction of the photomixing antenna. THz radiation is coupled into free space through a hyperhemispherical Si lens. Image courtesy of *Physical Domains, LLC*

2" beam by a 2" diameter 6" focal length gold coated off-axis parabolic mirror ($f\#=3$). A 2" 100mm focal length teflon focusing lens focused the beam through the sample and was then collected again by another 2" 100mm focal length teflon lens and collimated. The collimated light was gathered by another 2" diameter 6" focal length gold coated off-axis parabolic mirror. The off-axis parabolic mirror focused the collected THz radiation into the 6mm aperture of a Golay Cell.

The Golay Cell detects THz radiation by the expansion of a noble gas within a cell (typically Xenon, [19]). Heating caused by absorption of the THz radiation on a highly absorptive membrane with a mirror mounted on it causes the gas to expand within the cell and deflect a reference beam incident on a photocell inside the detector (**Figure 1-10**). By moving the beam incident on the photocell the current which it produces changes. The change in current is monitored and is indicative of a change in THz radiation. Since Golay Cell detection relies on the expansion of a noble gas it does not

differentiate between thermal emissions and THz radiation. Steps were taken to shield the Golay input aperture from all other radiating sources. The teflon lenses provide a buffer

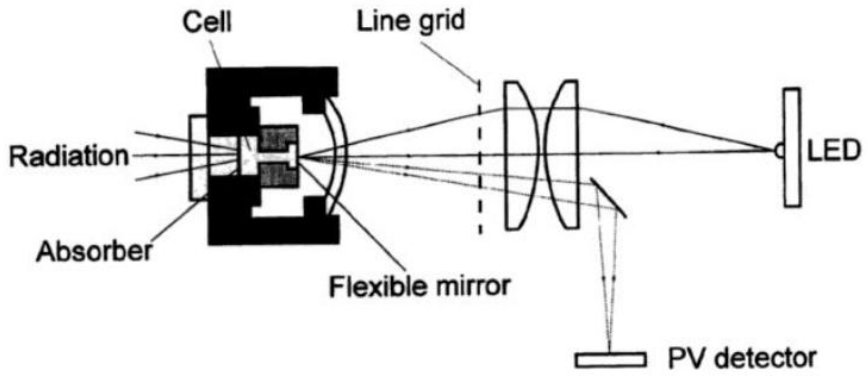

Figure 1-10: Diagram of a Golay cell. Incident radiation causes the expansion of a gas cell, deflecting light emitted from a LED which is detected by a photovoltaic detector. Figure taken from [19]

between the thermal emission of the antenna and the input of the Golay Cell. The Golay Cell was calibrated with a molecular gas laser at 20Hz and was shown to have a responsivity of 4.66kV/W. This detector lacks the ability to measure the phase and polarization components of the THz beam. However, since these details were not necessary for our experiments, the Golay Cell was the ideal detector. Also, unlike most detectors for these wavelengths, such as a Si bolometer or a Hot Electron Bolometer, the Golay Cell does not require cryogenics to operate.

A Stanford Research Systems lock-in amplifier was used to detect the output signal of the Golay Cell. The antenna bias was electrically chopped at 7Hz by a function generator with a 14V peak square wave output. Electrical chopping was chosen over optical chopping because it lowered the noise detected in the Golay Cell. The peak response of the Golay Cell used was found to be 7Hz for good SNR, requiring a 1s integration time of the signal.

The sample was contained within a closed cycle helium system which allowed the sample to be cooled to a minimum of 8K. The cryostat was outfitted with clear mylar windows on either side of the sample. Black poly-ethylene was used to cover the windows of the cryostat to prevent ambient light from hitting the sample. Finally, a set of quartz windows covered with diamond particles (diamond scatter windows) were mounted in front and behind the sample. These windows were used because they are held at the cold-finger temperature in order to reduce their thermal emission. The helium cryostat was mounted on an X-Y translation stage configuration which was controlled by computer via a serial interface (**Figure 1-11**). This allowed the sample to be scanned and imaged to locate its center. The output of the lock-in amplifier was collected by a data-acquisition system that was connected to a computer through an ethernet connection. Electrical connections to the sample were made via electrical feedthroughs in the cryostat and were controlled through the custom detector electronics.

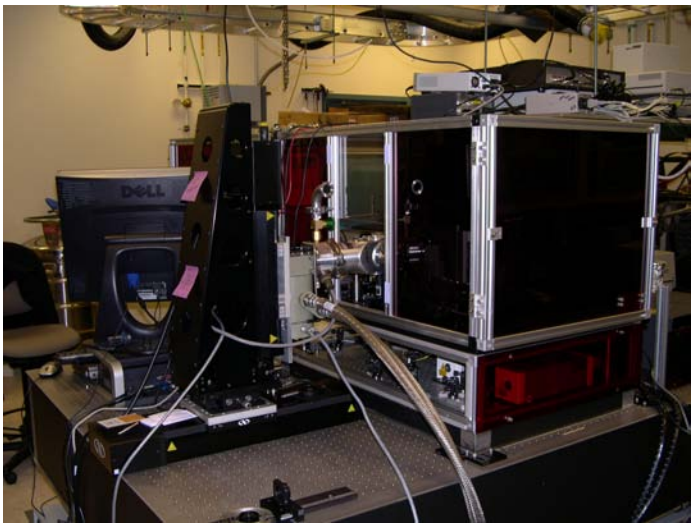

Figure 1-11: THz Photomixing Spectroscopy system. This picture shows the closed cycle system mounted on XY translation stages and inserted into the nitrogen purge box. The laser mixing system is located below the THz spectroscopy system, the two are coupled by single mode fiber.

The computer system and software allowed for simultaneous control of the wavelength of the lasers, the position of the cryostat, the electrical bias and detection of the sample, and the output of the signal magnitude of the lock-in amplifier.

1.4 System Characterization

To initially characterize the THz system it was necessary to compare wavelength scans from 0 to 1THz with known results from several publications. Water vapor has several unique absorption lines in the THz spectrum due to molecular vibrational resonances that have been well documented (**Figure 1-12**). In order to characterize the system, several high resolution scans were made between 0 to 1 THz measuring the water vapor content in the environment and compared with known absorption spectra. This measurement showed that the system was in fact working properly (**Figure 1-13**).

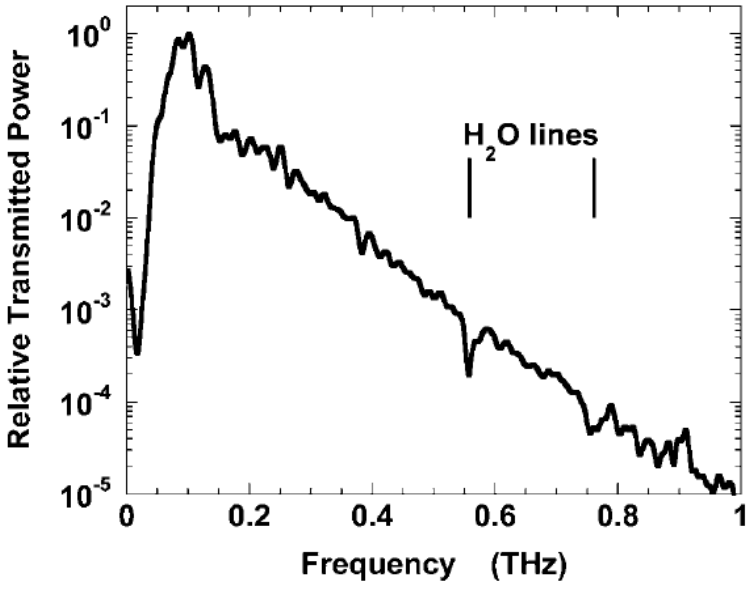

Figure 1-12: THz spectra showing the well documented water absorption feature at 0.56THz. Figure taken from [17].

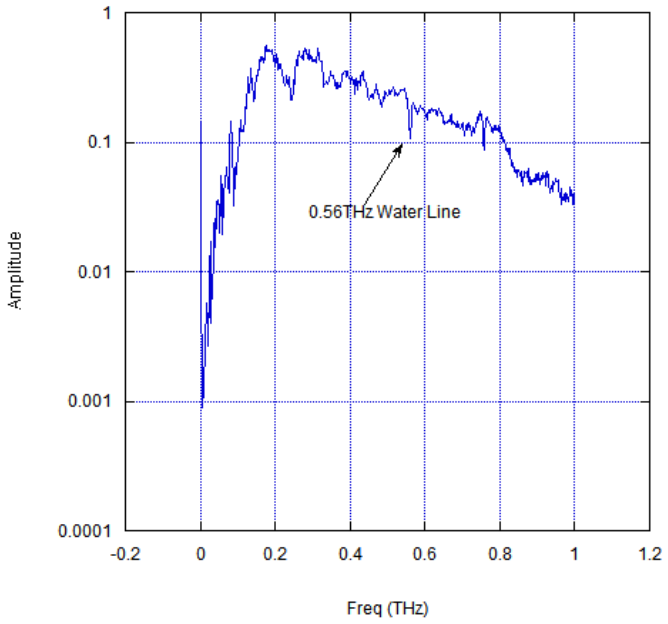

Figure 1-13: Measured THz spectra by the photomixing system from 0 to 1THz with the 560GHz water line identified in the spectra.

A high resolution scan (1GHz/step) of the 560GHz water line was made to verify our results (**Figure 1-14**). Although water vapor absorption is an excellent tool for characterization, for these experiments it is undesirable. In order to prevent attenuation of the signal the system was enclosed in a nitrogen purge box to lower the humidity around the THz system.

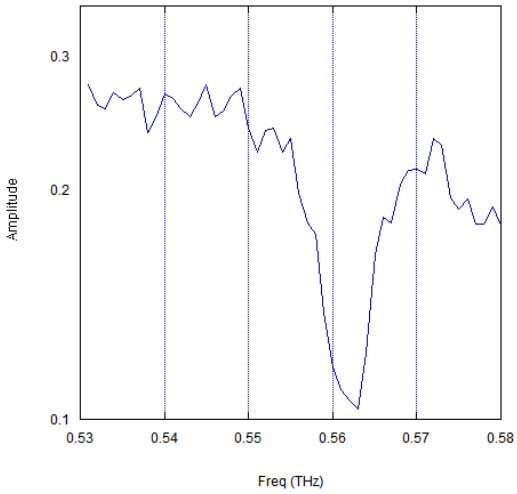

Figure 1-14: High resolution spectra (1GHz/step) of the 560GHz water absorption line

To characterize the THz beam a 3mm pinhole was mounted on the XY translation stage and scanned throughout the beam path after being collimated by the first off-axis parabolic reflector. Using custom imaging software a plot of the beam profile was created (**Figure 1-15**). The image taken shows a collimated beam that matched with predictions from the *f*# of the system ($f\#=3$). It was necessary to have a 2" collimated beam in order to reach the diffraction limit when focusing the THz beam with the teflon lenses through the sample.

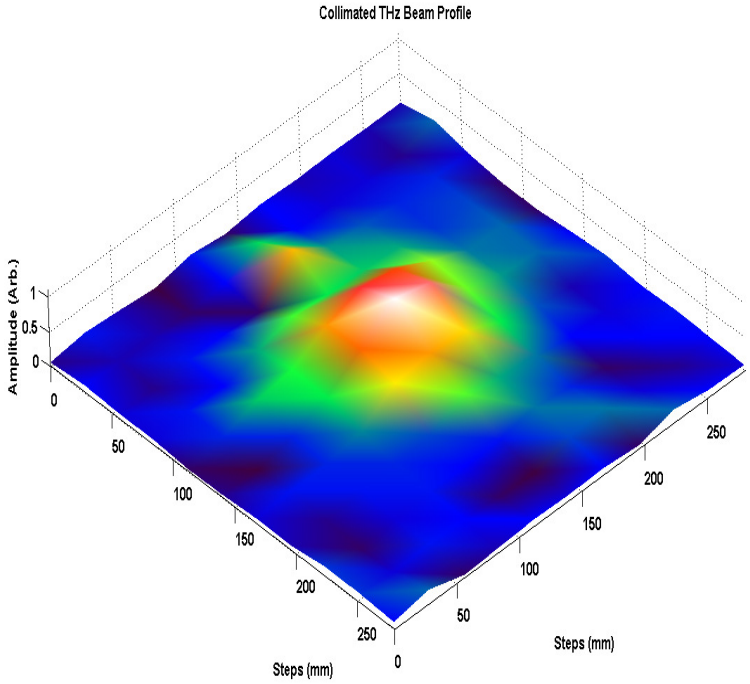

Figure 1-15: THz beam profile at 300GHz. This identified the beam as a 2" collimated Gaussian beam.

The maximum THz emission of the photomixer is centered around 300GHz. The system was tuned to this frequency and adjusted for maximum output power. With near perfect alignment the system was found to output a maximum power of ~ 4μW which

was within the specifications provided by the manufacturer of the photoconductive emitter.

It was also necessary to measure transmission through the sample header inside the cryostat. The sample header is a 16 pin DIP socket made from G-10 with a 1mm hole cut in the center. The sample header was also coated with reflective aluminum foil to block any transmission of THz radiation through the header except for that which was transmitted through the hole. First a scan was made to create an image of the THz transmission through the sample header. This provided a XY location for the center

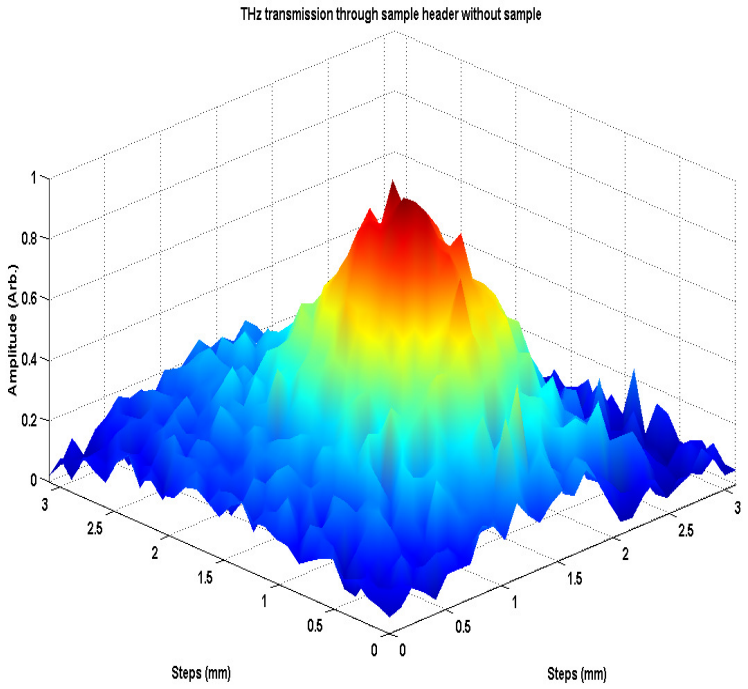

Figure 1-16: Image of THz transmission through the sample header showing a peak approximately 1mm in diameter.

of the sample header (**Figure 1-16**). While aligned at this position, 75% transmission of the incident beam was measured. Attenuation of the beam can be attributed to the absorption through the mylar and polyethylene films, diamond-scatter windows, and the focal size of the beam being larger than 1mm.

Chapter 2

Semiconductor Plasmons, Devices, and Dangling Issues

2.1 Bulk Plasmons

First introduced in 1900 by Paul Karl Ludwig Drude, the Drude model applies kinetic theory to describe electrical and thermal conduction in a metal. It is in this model that we first introduce the concept of an electron gas and also where we will begin our discussion of plasmons.

The molecules of a gas in a container are free particles that move in all directions, bouncing off the walls, and colliding with each other. Assume that each one of the molecules is a perfect solid sphere with a specific mass and direction of motion. In order to model the behavior of these molecules we must begin by making four basic assumptions:

1. Collisions are instantaneous and subsequently change the velocity of the particle.
2. Besides collisions, all interactions with other particles are neglected.

3. Every particle experiences a collision every τ, which we will refer to as the relaxation time.
4. The system can only reach thermal equilibrium through collisions.

With these postulates in place we can begin to apply simple Newtonian mechanics to the system.

Metals consist of atoms which have tightly bonded electrons to their nucleus called core electrons and loosely bonded electrons called valence electrons. The loosely bonded electrons are also referred to as conduction electrons and move about within the metal much like the molecules in a gas. If we consider these electrons as a system of electrons, we can refer to them as an electron gas.

Consider a time-dependent electric field of the form (for simplicity we will ignore the magnetic field for now)

$$\mathbf{E}(t,\omega) = \mathrm{Re}\left(\mathbf{E}(\omega)e^{-i\omega t}\right) \tag{2.1}$$

from kinetic theory we can describe the change in momentum of an electron in a metal as

$$\frac{d\mathbf{p}}{dt} = -\frac{\mathbf{p}}{\tau} - e\mathbf{E} \tag{2.2}$$

where $\boldsymbol{E}$ is the applied electric field, $\boldsymbol{p}$ is the momentum of the electron, e is the electron charge, $-e\boldsymbol{E}$ is the force exerted by an electric field, and τ is the relaxation coefficient [8]. We can arrive at the steady state solution for the differential equation, of the form

$$\mathbf{p}(t) = \mathrm{Re}\left(\mathbf{p}(\omega)e^{-i\omega t}\right) \tag{2.3}$$

By substituting the complex forms of (2.3) and (2.1) back into (2.2)

$$\frac{d\left(\mathbf{p}(\omega)e^{-i\omega t}\right)}{dt} = -\frac{\mathbf{p}(\omega)e^{-i\omega t}}{\tau} - e\left(\mathbf{E}(\omega)e^{-i\omega t}\right)$$

we arrive at

$$i\omega\mathbf{p}(\omega) = -\frac{\mathbf{p}(\omega)}{\tau} - e\mathbf{E}(\omega) \tag{2.4}$$

The current density is given by

$$J = -ne\mathbf{v}_{drift} \tag{2.5}$$

where v_{drift} is the particle drift velocity. The current density can be written as

$$\mathbf{J}(t) = \mathrm{Re}\left(\mathbf{J}(\omega)e^{-i\omega t}\right) \tag{2.6}$$

Momentum is given by

$$\mathbf{p} = m^*\mathbf{v}_{drift}$$

which can be rewritten as

$$\mathbf{v}_{drift} = \frac{\mathbf{p}}{m^*} \tag{2.7}$$

Substituting (2.7) back into (2.5) the current density becomes

$$\mathbf{J}(\omega) = -\frac{ne\mathbf{p}(\omega)}{m^*} \tag{2.8}$$

Solving (2.4) for the momentum

$$\mathbf{p}(\omega) = -\frac{e\mathbf{E}(\omega)}{\frac{1}{\tau} - i\omega} \tag{2.9}$$

Equation (2.8) then becomes

$$\mathbf{J}(\omega) = -\frac{ne}{m^*}\left(-\frac{e\mathbf{E}(\omega)}{\frac{1}{\tau} - i\omega}\right) = \left(\frac{\left(\frac{ne^2}{m^*}\right)\mathbf{E}(\omega)}{\frac{1}{\tau} - i\omega}\right) \tag{2.10}$$

The general form of current density is written as

$$\mathbf{J}(\omega) = \sigma(\omega)\mathbf{E}(\omega) \tag{2.11}$$

where $\sigma(\omega)$, because of its frequency dependence, is known as the AC conductivity. Rewriting (2.10) we are given an expression for the current density as a function of the electric field $\boldsymbol{E}$, and the angular frequency ω

$$\mathbf{J}(\omega) = \left(\frac{\left(\frac{ne^2\tau}{m^*} \right)\mathbf{E}(\omega)}{1 - i\omega\tau} \right) \tag{2.12}$$

Therefore, the AC conductivity is given by

$$\sigma(\omega) = \frac{\frac{ne^2\tau}{m^*}}{1 - i\omega\tau} = \frac{\sigma_0}{1 - i\omega\tau} \tag{2.13}$$

where σ_0 is given as the DC conductivity.

Now we will consider a propagating electromagnetic field within a metal. The force on an electron from an electromagnetic field is given by the Lorentz Force

$$\mathbf{F}_{Lorentz} = -e\left(\mathbf{E} + \mathbf{v}_{inst} \times \mathbf{B}\right)$$

where $\boldsymbol{E}$ is the electric field vector, $\boldsymbol{v}_{\text{inst}}$ is the instantaneous velocity, and $\boldsymbol{B}$ is the magnetic field. Then from (2.4) we have

$$i\omega\mathbf{p}(\omega) = -\frac{\mathbf{p}(\omega)}{\tau} - e\mathbf{E}(\omega) - \frac{e\mathbf{p}}{m^* c} \times \mathbf{B} \tag{2.14}$$

However, the last term in (2.14) is negligible because $-e\mathbf{p}/m^* c \times \mathbf{B} \ll \mathbf{E}$ due to the $\mathbf{p}/c$ term. Therefore we can proceed with our results of (2.13) and the differential form of Maxwell's equations can be written as

$$\begin{aligned}
\nabla \cdot \mathbf{D} &= \rho_{free} \\
\nabla \cdot \mathbf{B} &= 0 \\
\nabla \times \mathbf{E} &= -\frac{1}{c}\frac{\partial \mathbf{H}}{\partial t} \\
\nabla \times \mathbf{H} &= \frac{1}{c}\frac{\partial \mathbf{H}}{\partial t} + \frac{4\pi}{c}\mathbf{J}
\end{aligned} \tag{2.15}$$

where

$$\mathbf{E}(t) = \mathrm{Re}\left(\mathbf{E}(\omega)e^{-i\omega t}\right)$$
$$\mathbf{H}(t) = \mathrm{Re}\left(\mathbf{H}(\omega)e^{-i\omega t}\right)$$

Since we are considering an electromagnetic wave the free charge density, ρ_{free}, is zero.

Faraday's Law can be written as

$$\nabla \times \mathbf{E} = -\frac{i\omega}{c}\mathbf{H} \tag{2.16}$$

Taking the curl of both sides

$$\nabla \times \left(\nabla \times \mathbf{E}\right) = -\frac{i\omega}{c}\left(\nabla \times \mathbf{H}\right)$$

leads us to

$$-\nabla^2 \mathbf{E} = -\frac{\omega^2}{c^2}\left(1 + \frac{4\pi i\sigma}{\omega}\right)\mathbf{E} \tag{2.17}$$

This form of (2.17) is known as the Helmholtz wave equation for the electric field. Let

$$\varepsilon(\omega) = 1 + \frac{4\pi i\sigma}{\omega} \tag{2.18}$$

where $\varepsilon(\omega)$ is the complex dielectric constant. At high frequencies we have

$$\omega\tau \gg 1 \tag{2.19}$$

and (2.13) can be approximated by

$$\sigma(\omega) = -\frac{\left(\frac{ne^2}{m^*}\right)}{i\omega}$$

Therefore (2.18) becomes

$$\varepsilon(\omega) = 1 - \frac{\omega_p^2}{\omega^2} \tag{2.20}$$

where

$$\omega_p^2 = \frac{4\pi ne^2}{m^*} \tag{2.21}$$

and ω_p is known as the plasmon frequency. Plugging (2.20) back into the Helmholtz wave equation (2.17) we see that when $\varepsilon(\omega)$ is positive (when $\omega > \omega_p$) we have an oscillatory solution which makes the electron gas transparent and allows radiation to propagate through it. When $\varepsilon(\omega)$ is negative (2.17) gives a solution of the form of a decaying exponential causing the incident radiation to be absorbed.

Above we derived the expression for the plasmon frequency at which an incident electric field is either reflected or transmitted. When an electron gas is displaced from the positively charged ion cores within the material it generates an electric field which acts as a restoring force to pull the system back to equilibrium, [3], given by

$$E = \frac{ne\Delta y}{\varepsilon_0 \varepsilon_r} \tag{2.22}$$

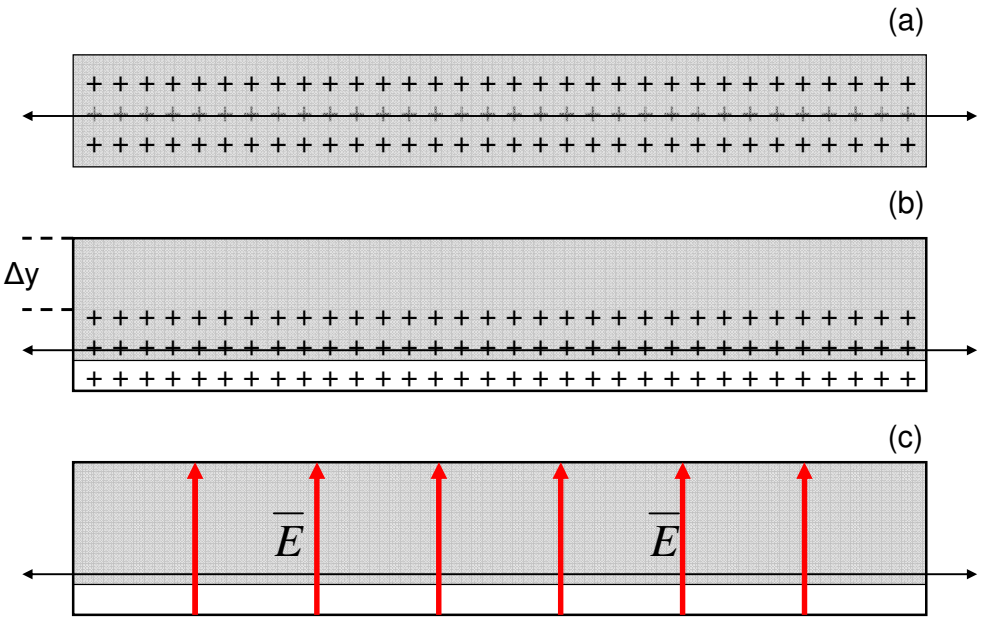

Figure 2-1: Bulk Plasmon Oscillation in a metal. (a) System in equilibrium (b) Electron gas displacement (c) Electric field acting as the restoring force

where Δy is the displacement of the electron gas (**Figure 2-1**). It is this oscillating electric field generated by an oscillating displacement of the electron gas which we define as a bulk plasmon.

2.2 Two-Dimensional Semiconductor Plasmons

The term *two-dimensional electron gas* (2DEG) refers to the electron gas described in the previous section which is restricted to movement in only two dimensions. This is the fundamental idea behind such devices as the field-effect transistor in which an inversion layer charge density of carriers is accumulated at the oxide-semiconductor interface when the gate is biased beyond the built-in threshold voltage of the device. This inversion layer of charge is pinned in the oxide-

semiconductor interface direction but is permitted to move about laterally in the other two spatial directions in the device.

The theory of generation of a plasmon oscillation within a two-dimensional layer is much more complicated to derive than the three-dimensional bulk plasmon concept which we arrived at through the Drude Model in the previous section. This concept can often be found in advanced texts on solid state physics in discussions of Lindhard screening [1]. However, the general ideas of a plasmon which we defined are still valid and can be applied to the semiconductor plasmon.

We described previously that a plasmon oscillation is a sea of conduction electrons with a resonant frequency at which the sea oscillates back and forth with respect to the positively charged ion cores of the material, (2.21). In a two-dimensional channel this plasmon frequency is given by

$$w_p(\mathbf{q}) \cong \sqrt{\frac{e^2 n \mathbf{q}}{2\varepsilon_0 \varepsilon_r m^*}} \qquad \text{(MKS)} \qquad (2.23)$$

where n is the electron density, ε_r is the relative permeability of the material, m^* is the effective mass of the conduction electron, and $\boldsymbol{q}$ is a two-dimensional wave vector in the plane of the 2DEG [2]. Immediately we see that this definition departs from the 3D case due to the plasmon oscillation now being dependant on both a carrier density and a wave-vector. This difference arises from the fact that although the electron gas is now two-dimensional the restoring force from the electric field remains three-dimensional which creates a fringing effect on either side of the inversion layer. This is the key concept behind 2DEG plasmon oscillations in semiconductors and also the driving force behind the research conducted in this thesis.

2.3 Observations of 2D Plasmons in Semiconductors

Two-dimensional plasmons in semiconductors were first observed in 1978. Commonly referred to is the work done by S.J. Allen et. al. in which two-dimensional surface plasmons in semiconductors were first investigated in silicon. Although discovered 30 years ago, even today a great deal is left unexplored in terms of two-dimensional plasmon transport.

Figure 2-2 is a cross sectional diagram of a metal-insulator semiconductor field-effect transistor (MISFET) used to couple radiation to plasmon resonances in a semiconductor. It turns out that two-dimensional plasmons do not naturally couple to radiation due to severe wave-vector mismatches [13]. The metallic grating pattern on this device modulates the incident electromagnetic radiation in order to facilitate optical coupling. Because of the layout of this grating structure, only radiation that is polarized perpendicular to the grating is absorbed into the semiconductor plasmon; radiation polarized parallel does not get spatially modulated in the correct way to excite plasmons. The grating structure of this device is designed such that the periodicity of the grating determines the electromagnetic wave oscillation coupling to the plasmon oscillations in the 2DEG. The spacing of the grating fingers is such that far-infrared light is coupled to the plasmons with wave vectors

$$\mathbf{q} = \frac{2\pi n_q}{\delta}; \quad n_q = 1, 2, 3, ... \tag{2.24}$$

where n_q is the mode index (not to be confused with the electron density of the inversion

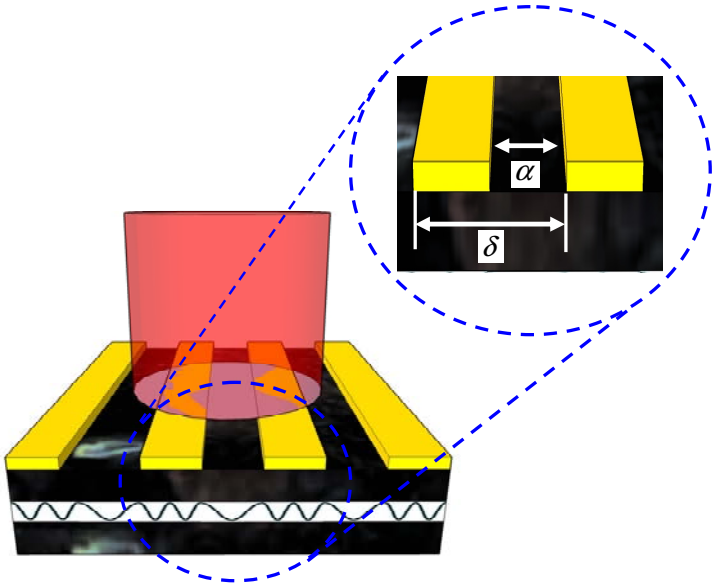

Figure 2-2: Split Grating MISFET with an incident electromagnetic wave, showing grating period and spacing

layer) and δ is the grating period. Equation (2.24) is then used to determine the plasmon frequency of oscillation, given in (2.23).

Another important discovery of the work done by S.J. Allen et al. [13] is the effect of electron densities in the inversion layer on the plasmon resonances of the device. It was discovered that with large electron densities, $>10^{12}cm^{-2}$, the experimental data directly correlated with the theoretical model further confirming the concept of plasmon oscillations in the semiconductor.

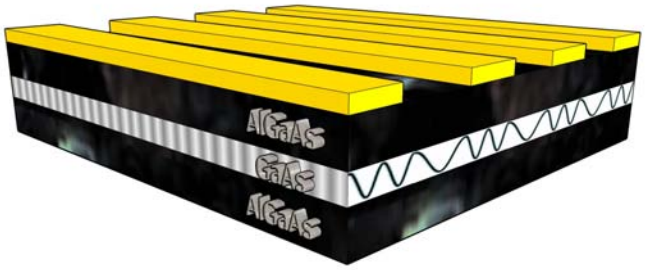

Figure 2-3: Plasmon oscillations in a MISFET

2.4 Grating Gate Detectors

There is a large initiative to improve the detection methods of terahertz radiation. Current methods of detection suffer from the common problem of slow response characteristics. Other issues contribute to the drawbacks of these detectors such as sensitivity, resolution, use of cryogens, size, and frequency selectivity. Finding an alternative method for detection of terahertz radiation is a common theme for researchers in this field of study.

THz detection using a quantum-well (QW) grating-gated field-effect transistor (FET) by excitation of plasmon modes has been shown as a viable high-speed alternative to the techniques currently available. These devices offer a high-speed, high-resolution, and frequency-selective alternative to existing technology. However, the physical properties behind their operation are not completely understood. By fully understanding these physical properties these devices may potentially outperform current THz detector technology.

The devices used in this thesis were grown by molecular beam epitaxy to generate a GaAs-AlGaAs heterostructure consisting of a single 40nm wide GaAs quantum well 200nm below the surface of the wafer (**Figure 2-4**) [2]. The grating-gate was created by metallization of 20nm Ti and 50nm Au on the surface of the device. The source and drain of the FET were annealed to create ohmic contacts. These devices were fabricated in a split-gate configuration (**Figure 2-5**) which allows the source and drain regions to be pinched off from each other enhancing the responsivity of the device, [9], but this feature was not used in these experiments and all gates were operated as a single gate. The grating period for this device was $\delta = 4\mu m$ with a 50% duty cycle, including the finger

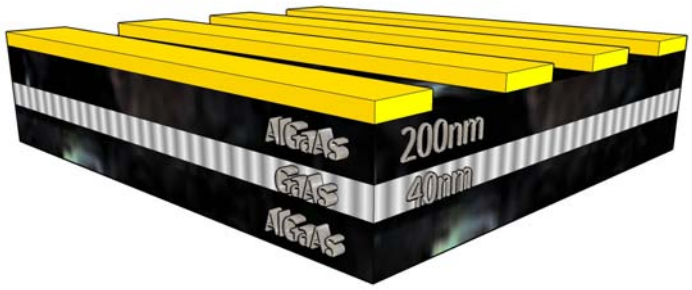

Figure 2-4: Single-QW GaAs-AlGaAs heterostructure showing the depth of the QW structure from the wafer surface

gate. Measured at 4K, the mobility of the QW was $\mu \approx 5 \times 10^6\ cm^2/(V\text{-}s)$, and had an electron density of $n = 2.5 \times 10^{11}\ cm^{-2}$, as is detailed in [9]. As in (2.23), this device was shown to have tunable plasmon modes at

$$w_p\left(V_G, \mathbf{q}\right) \cong \sqrt{\frac{e^2\, \mathrm{n}\left(\mathrm{V_G}\right)\mathbf{q}}{2\varepsilon_0 \varepsilon_r m^*}} \tag{2.25}$$

where $n(V_G)$ is the density of carriers under the grating lines controlled by the bias voltage of the gates. A negative applied voltage to the grating gates reduces the channel conductance, making this a depletion mode device.

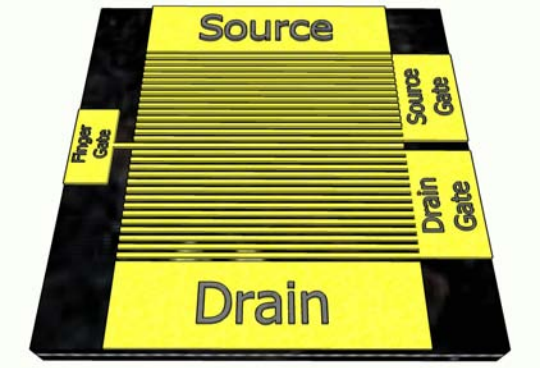

Figure 2-5: Diagram of a split-grating QW FET plasmonic terahertz detector. The split-grating configuration allows the source and drain regions to be pinched off from each other to enhance the responsivity of the device.

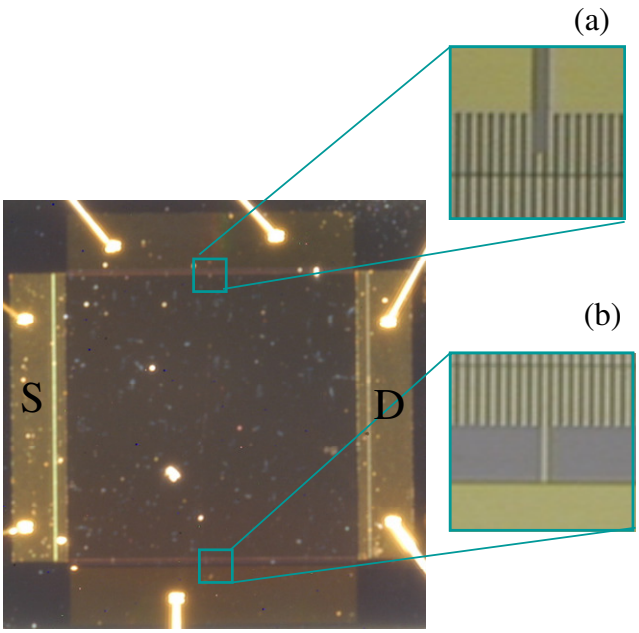

Figure 2-6: Image of a split -grating-gate plasmonic terahertz detector (a) shows the position of the finger gate (b) shows independent source and drain gate

2.5 Survey of Surface Plasmons in Single-QW Grating-Gated Terahertz Detectors

Although two-dimensional surface plasmons were first observed over thirty years ago we have yet to fully understand their physical properties and how they relate to the photoresponse in grating-gated terahertz detectors. By studying electron scattering, electromagnetic wave coupling, reflectivity and absorption we may begin to reveal the mechanism behind their operation.

It was the purpose of this research to understand the transmission characteristics of surface plasmons with respect to frequency. It has been shown that dips in the transmission spectrum of the device as a function of the gate voltage directly correspond to plasmon resonances in the 2DEG. However, we show that not only does the position of these resonant transmission minima change as a function of frequency but also the

depth. These results provide insight into the physical properties of these plasmon resonances which is critical in making advances in this technology.

Chapter 3

Photomixing Spectroscopy of Two-Dimensional Plasmons

3.1 Initial Characterization

Observations of plasmon resonance shift with temperature have been observed as temperature was increased from 20K to 70K [9]. Therefore experiments done on this device were performed at 20K where the plasmon resonance was shown to be stable. The device was mounted on a cold finger inside of a continuous flow helium system and cooled to 20K. The cryostat was mounted on a translation stage and an image was taken to identify peak center of the device (**Figure 3-1(a)**). Measurements were made of the devices I-V characteristics without illumination to verify that the device was working properly. As voltage is increased towards pinch-off (V_g = -0.7) in the source-gate and drain-gate the device becomes more resistive due to depletion of carriers in the conduction channel (**Figure 3-1(b) and (c)**). The finger-gate is shown to have little effect on the conductivity of the device (**Figure 3-1(d)**). As the gates were ramped down data was taken to verify that the channel returned to equilibrium at V_g = 0V.

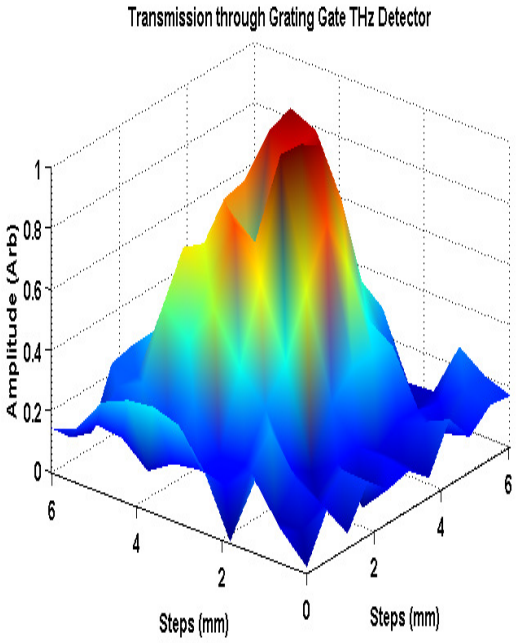

(a)

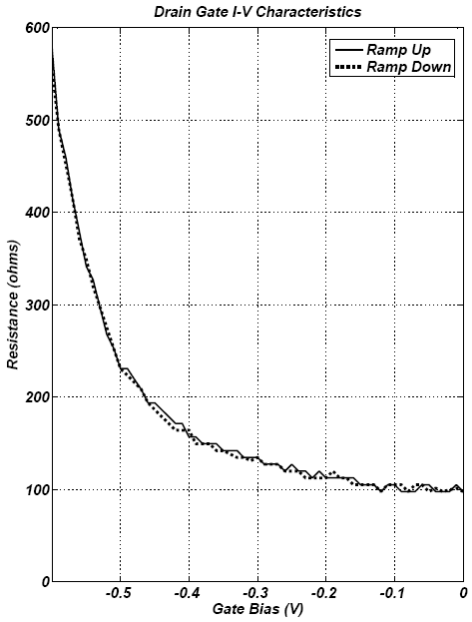

(b)

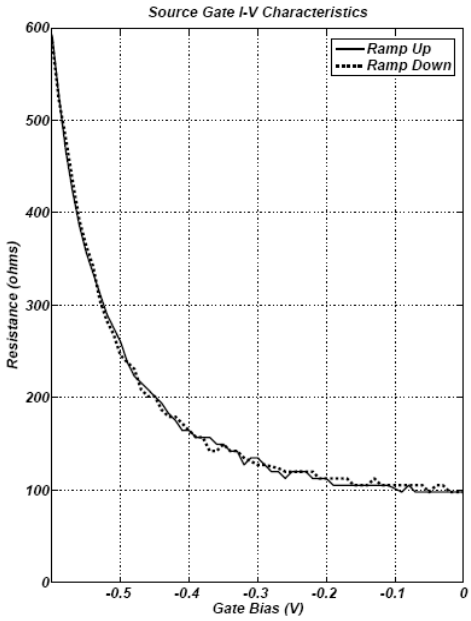

(c)

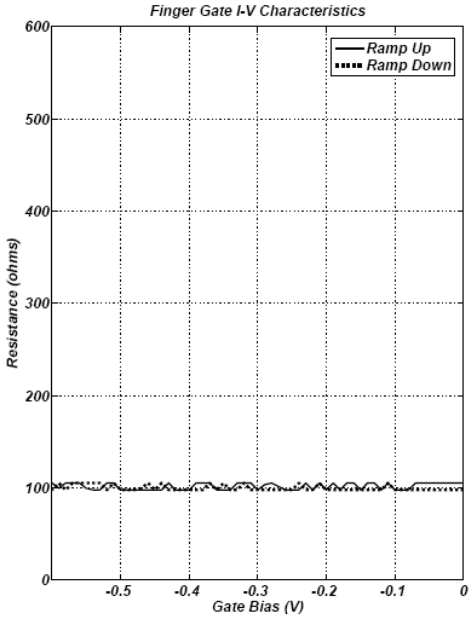

(d)

Figure 3-1: Plots of the device characteristics (a) Transmission image of the sample in the cryostat (b) Drain-Gate IV Characteristics (c) Source-Gate IV Characteristics (d) Finger-Gate IV Characteristics

3.2 Results and Conclusions

Data were taken at three different frequencies and plotted as a function of the gate-bias voltage with the source and drain voltages at zero (**Figure 3-2**). As the incident radiation is tuned towards higher frequencies the plasmon resonance is shifted towards less negative gate voltages. Local minima in the transmission spectrum identify locations of plasmon resonances within the quantum well.

Although transmission measurements are classically performed to measure absorption within a medium, we have found evidence that more careful measurements must be made to attribute absorption to the local minima in the transmission spectrum. We consistently found that transmission did not return to the initial background transmission level with increased negative gate bias after peak plasmon resonance. This result implies one of two things:

1. Background absorption is different before and after plasmon resonance.
2. The amount of light reflected off the sample changes before and after resonance.

A change in background absorption is not consistent with photoresponse measurements, while a change in reflection due to changes in the index of the material is feasible for any material. Therefore, to truly understand this result, simultaneous measurements of both transmission through and reflection off the sample must be made.

From the design parameters of the grating-gated THz detector in **Table 3-1** and (2.23) we can calculate the ungated plasmon resonance, shown in (3.1). The plot in **Figure 3-2** shows that when the frequency of incident radiation is approximately equal to

the ungated plasmon resonance (as given by the grating period) the amount of transmission is significantly less than when frequency is above this resonance.

Table 3-1: Design parameters for grating-gated THz detector

Property	Value	Units (MKS)
Electron Density (n)	2.5×10^{15}	m^{-2}
Dielectric Constant (ε_r)	12.85	
Effective Mass (m^*)	$0.067\left(9.1\times10^{-31}\right)$	*Kg*
Electron Charge (*e*)	1.602×10^{-19}	*Coulomb*
Grating Period (δ)	4×10^{-6}	*M*

$$\mathbf{q} = \frac{2*\pi*n_q}{\delta} = \frac{2*\pi*1}{4\times10^{-6}m} = 1570796.3$$

$$w_p^2 = \frac{e^2 n\mathbf{q}}{2\varepsilon_o\varepsilon_r m^*} = \frac{\left(1.602\times10^{-19}\right)^2\left(2.5\times10^{15}m^{-2}\right)\left(1570796.3\right)}{2\left(12.85\right)\left(8.85\times10^{-12}\right)\left(0.067\left(9.1\times10^{-31}\right)\right)} \qquad (3.1)$$

$$w_p = 2.6959\times10^{12}\,rads$$

$$f_p = \frac{w_p}{2\pi} = \frac{2.6959\times10^{12}\,rads}{2\pi} \cong 430GHz$$

Plasmon interactions between (ungated plasmons) the gratings are different to those underneath (gated plasmons). Until now it was not understood how these different plasmons interrelate. As the frequency of the incident radiation approaches that of the ungated resonance, as shown in (3.1), there is strong coupling of both the ungated and gated plasmons causing light transmission through the sample to be significantly lower than as seen at higher frequencies (**Figure 3-2**). By changing the period of the grating the ungated plasmons resonance can be shifted to different frequencies. This allows detectors to be designed to have large plasmon resonances at different frequencies, modifying the peak operation of the detector. The bandwidth of this response is unknown at this time, but once found this may allow us to design broadband detectors around the ungated plasmon resonance.

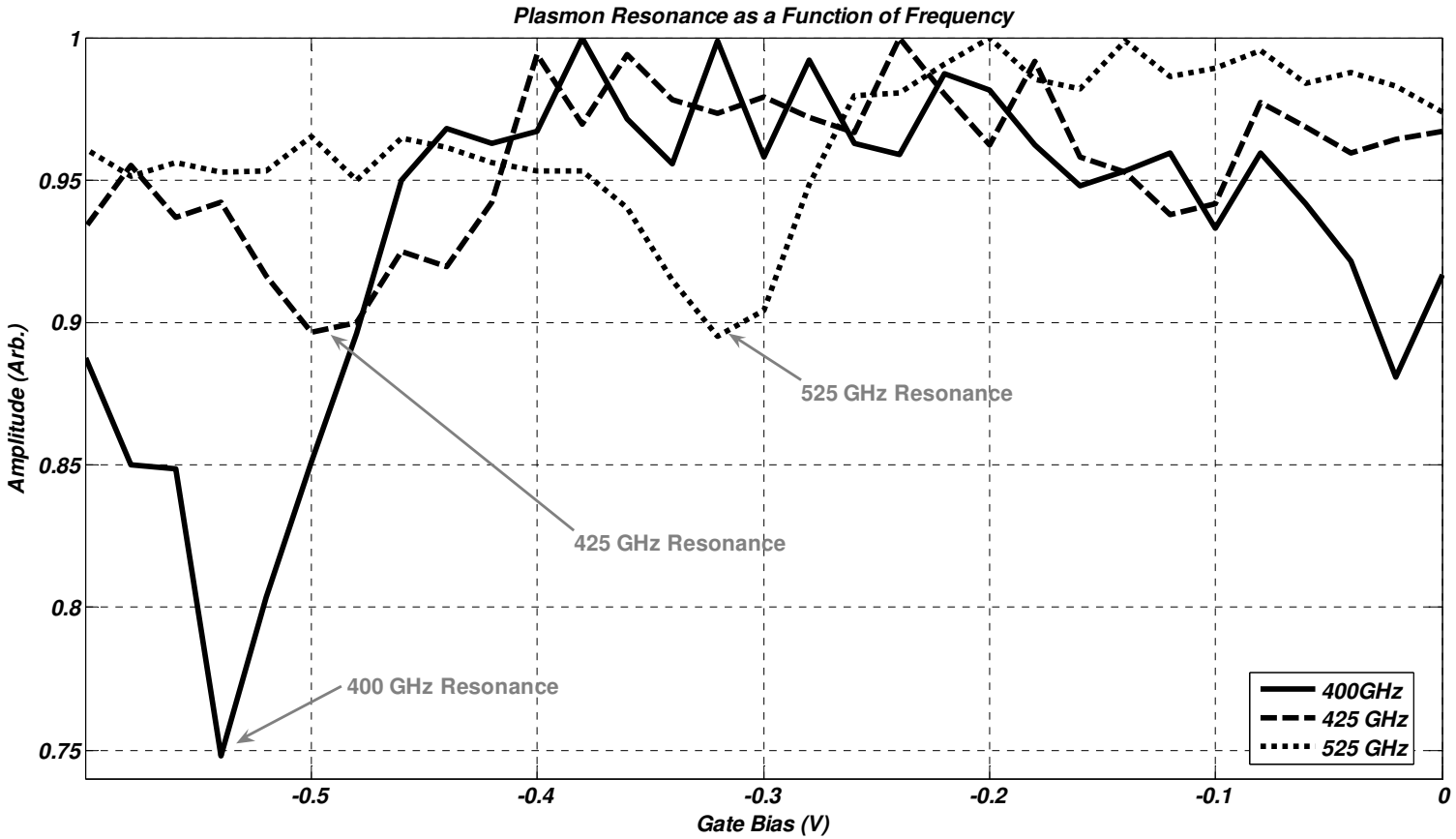

Figure 3-2: Transmission through the grating-gated plasmon terahertz detector as a function of frequency. Local minima in the plot correspond to plasmon resonances at each frequency. Note that after resonance the transmission *does not* return to the original level.

The plasmon resonances in these grating-gated terahertz plasmon detectors have been shown to be both electrically tunable and, in theory, infinite in number. Access to this large number of resonances demonstrates this device's usefulness in detecting terahertz radiation. It may be found in the future that particular plasmon modes persist to higher temperature while others may exhibit higher sensitivity. Through these experiments we have discovered that the properties of the detector change after the peak plasmon resonance. This result is most likely attributed to an index change in the material properties and needs to be investigated further. **Figure 3-3** shows an example of how transmission can be altered by an index change. We have also shown that as we approach the ungated plasmon resonance of the detector there is apparently stronger coupling of the electromagnetic field to the plasmon resonance. As the ungated and gated plasmon resonances are brought into coincidence there is likely a strong coupling of the two different plasmons leading to increased absorption. Without investigating further it is unknown whether the reflectivity of the material changes as a function of frequency (as **Figure 3-3** implies). However, this phenomenon is common in dielectrics, metals, and semiconductors and is most likely the case for these detectors.

As noted thus far, two new things have been observed in the grating gated detectors. Reflectance of this device likely changes and absorption appears stronger when gated and ungated resonances are near coincidence. The latter is particularly important as previous photoresponse measurements where performed far from this region [2, 11]. The photomixing spectroscopy performed to date is

only a starting point for improving detector performance; nonetheless, it has already revealed new information. In future years, this system will not only allow for characterization of plasmon resonances, but it will also permit new radiation coupling structures to be designed and tested. Without such a system having extreme frequency tunability this work would largely need to proceed as a series of educated guesses which are costly, inefficient, and unreliable. When possible, it is always better to understand the physical mechanisms behind a device.

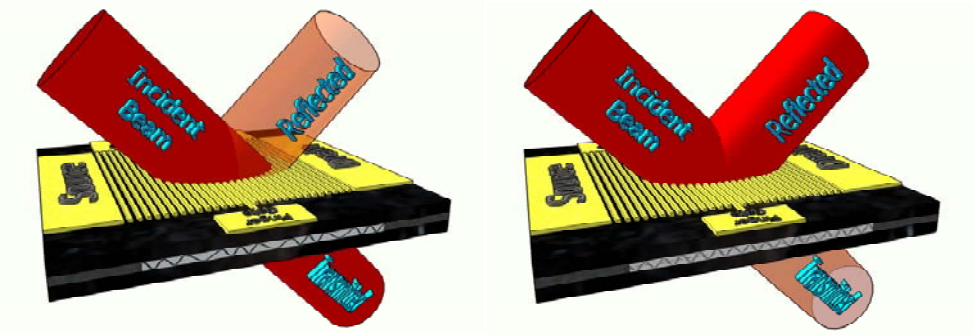

(a) (b)

Figure 3-3: Diagram of the theoretical beam transmission and reflection (a) Transmission and reflection off of sample when the incident radiation is greater than the ungated response of the plasmon resonance (f >400GHz for this detector). (b) Transmission and reflection off of sample when the incident radiation is equal to the ungated plasmon resonance. It is unknown whether light is reflected (due to index change) more strongly at this frequency.

Chapter 4

Future Work

4.1 Transmission and Reflectivity

Tremendous time and thought was put into the design and implementation of the terahertz spectroscopy system used in this work. However, the difficulty of the work performed in this thesis has revealed a number of improvements to the system that would aid in our future research goals. As research into the physical properties of two-dimensional plasmons is far from complete, we feel the implementation of these improvements will increase our understanding of this physical phenomenon.

In order to further understand the results of these experiments we must make modifications to the system to enable us to measure both transmission and reflection simultaneously. From the results in Chapter 3 it was shown that the transmission through the detector does not return to its original amplitude after a plasmon resonance. Without measuring the reflectivity of the device it is not possible to completely understand the mechanism behind this change; essentially, transmission alone cannot be ascribed to absorption. It is believed at this time that after the plasmon resonance the index of the

material changes such that more light is back reflected off the sample. It is also unknown how much light is reflected on-resonance. By modifying the current system we will be able to measure this property more carefully.

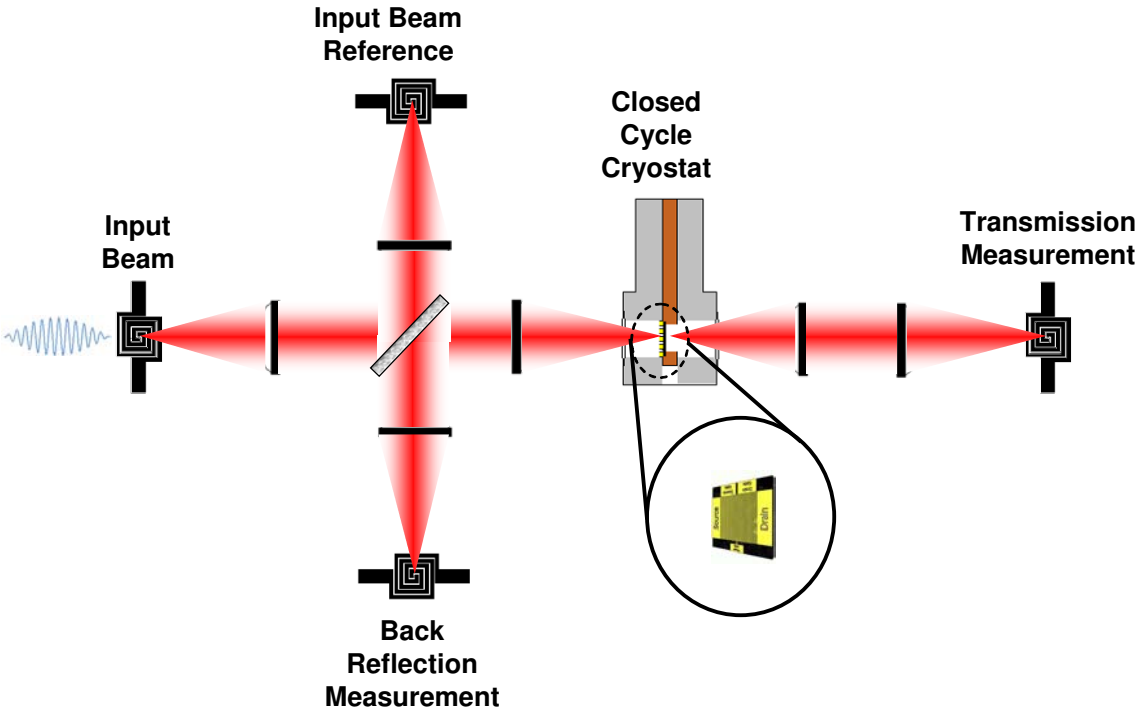

Figure 4-1: Transmission and reflectivity terahertz spectroscopy system. This is system is an all lens system for ease of alignment. This system also employs the use of an input reference measurement for noise cancelation purposes.

Shown in **Figure 4-1** is a system for simultaneously measuring transmission and reflectivity of a sample. There are three unique changes that set this system apart from the original setup, namely, the use of homodyne detection (using antennas for detection), sampling of the input beam, and elimination of reflective optics.

Teflon lenses have proven very difficult to use for these experiments. Although they are typically the cheaper alternative to lensing for these wavelengths they suffer from a number of drawbacks such as chromatic aberration (changing the focal distance as

a function of frequency) and attenuation. Therefore we have researched other materials to use. Picarin plano-convex lenses have been shown to be excellent for these wavelengths of light. Although they are considerably more expensive than teflon there is little or no chromatic aberration, a larger variety of focal lengths, very little attenuation, and they pass visible wavelengths aiding in the alignment of the system.

As light enters the system from the input antenna it is split into two directions from a mylar beam-splitter. One beam is sent into an antenna which samples the input beam for noise cancelation purposes, the other beam is sent into the front facet of the sample. The use of an antenna for detection purposes works on the same principles as emission. However, the antenna is no longer biased to create an electric field to accelerate the carriers. Instead the potential across the antenna directly corresponds to the strength of the incident radiation and is measured by a lock-in amplifier. This technique is commonly used in time-domain spectroscopy systems and allows for high-speed detection of the signal.

When the terahertz radiation hits the sample, part of the beam is transmitted through it and the rest is reflected. The transmitted beam is detected on the other side of the sample by the same homodyne technique used in the input beam measurement. The reflected beam is sent backwards through the system until it reaches the 50:50 beam-splitter and is then sent into an antenna which measures the strength of the reflection.

An added benefit to this configuration is the ability to perform rotation and angle-resolved measurements which allow us to measure polarization response and light diffraction of the sample which may help to reveal other unknown physical properties of plasmons. However, it should be noted that homodyne measurements are very difficult

to perform and require very precise alignment of the optics. Therefore, an alternative to this method was devised and is shown in **Figure 4-2**.

In the configuration shown in **Figure 4-2** both transmission and reflectivity are

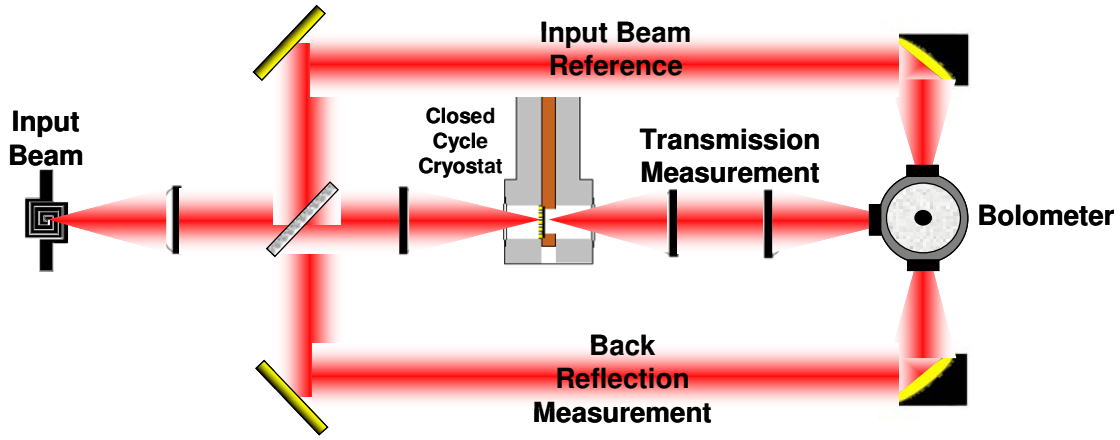

Figure 4-2: Transmission and reflectivity measurements using mostly reflective optics and a tri-measurement bolometer.

measured, but rotation and angle-resolved measurements can no longer be made. However, by using mostly reflective optics, although more difficult, the amount of attenuation of the beam is lessened. The bolometer used in this configuration has three separate Si detectors located 90-degrees from each other. The benefit to this bolometer is that all the detectors are held at the same temperature and therefore the measurements do not suffer from temperature differentials at the detectors, thus lessening noise fluctuations.

4.2 Experiments

The results reported in this thesis have not only revealed unknown properties of these single-QW grating-gated plasmonic terahertz detectors but they have also uncovered previously unknown phenomena. Initially experiments must be done to

understand the reflectivity and transmission of this device as a function of frequency. Although we feel that these experiments will uncover a great deal about the physical properties of this device, this by no means will unveil everything that needs to be understood.

Experiments such as temperature characterization and photoconductivity will also be beneficial in understanding device characteristics and plasmon scattering mechanisms and will help in improvement of the design of this device for detection of terahertz radiation. Eventually we hope to create a high speed device that will operate at near room temperature with a low noise-equivalent power (NEP). Indeed, such a detector would allow high-speed terahertz imaging, high resolution spectroscopy, and ultimately enhance our understanding of the terahertz regime of the electromagnetic spectrum.

References

[1] J.H. Davies, *The Physics of Low-Dimensional Semiconductors* (Cambridge University Press, New York, NY, 1998), p. 356.

[2] E.A. Shaner, M. Lee, M.C. Grine, A.D. Grine, J.L. Reno, S.J. Allen, *Single-quantum-well grating-gated terahertz plasmon detectors*, Applied Physics Letters **87**, 193507 (2005).

[3] J.E. Bjarnason, *Terahertz Photomixing Spectrometer Technology*, Ph.D. Dissertation, University of California Santa Barbara, (2007).

[4] C. Kittel, *Introduction to Solid State Physics* (John Wiley & Sons, Inc., New York, NY, 1996), p. 270-290.

[5] D.A. Neamen, *Semiconductor Physics and Devices* (McGraw Hill Publishing, New York, NY, 2003), p. 351-354.

[6] M. Lee, M.C. Wanke, and J.L. Reno, *Millimeter wave mixing using plasmon and bolometric response in a double-quantum-well field-effect transistor*, Applied Physics Letters **86**, 033501 (2005).

[7] E.R. Brown, A.W.M. Lee, B.S. Navi, and J.E. Bjarnason, *Characterization of a Planar Self-Complementary Square-Spril Antenna in the THz Region*, Microwave and Optical Technology Letters **85**, 3 (2006).

[8] A.I. Galuza and A.B. Beznosov, *Optical functions of the Drude model: transformations of the spectra over wide ranges of parameters*, Low Temperature Physics **27**, 3 (2001).

[9] E.A. Shaner, A.D. Grine, M.C. Wanke, M. Lee, J.L. Reno, and S.J. Allen, *Far-Infrared Spectrum Analysis Using Plasmon Modes in a Quantum-Well Transistor*, IEEE Photonics Technology Letters **18**, 18 (2006).

[10] X.G. Peralta, S.J. Allen, M.C. Wanke, N.E. Harff, J.A. Simmons, M.P. Lilly, J.L. Reno, P.J. Burke, J.P. Eisenstein, *Terahertz photoconductivity and plasmon modes in double-quantum-well field-effect transistors*, Applied Physics Letters **81**, 9 (2002).

[11] E.A. Shaner, M.C. Wanke, A.D. Grine, S.K. Lyo, J.L. Reno, and S.J. Allen, *Enhanced responsivity in membrane isolated split-grating-gate plasmonic terahertz detectors*, Applied Physics Letters **90**, 1 (2007).

[12] E.R. Brown, *THz generation by photomixing in ultrafast photoconductors*, International Journal of High Speed Electronics and Systems **13**, p. 497-545, 2003.

[13] S.J. Allen, D.C. Tsui, R.A. Logan, *Observation of the Two-Dimensional Plasmon in Silicon Inversion Layers*, Physics Review Letters **38**, 17 (1977).

[14] N. Ashcroft, N.D. Mermin, *Solid State Physics* (Harcourt Brace College Publishers, Orlano, Fl., 1976), p. 1-20.

[15] F.L. Pedrotti, S.J., L.S. Pedrotti, *Introduction to Optics* (Prentice Hall, Upper Saddle River, NJ, 1993), p. 196.

[16] S.M. Wentworth, *Fundamentals of Electromagnetics with Engineering Applications* (John Wiley & Sons, Inc., New York, NY, 2005), p. 210-214.

[17] M.S. Brown, G.J. Fiechtner, J.V. Rudd, D.A. Zimdars, M. Warmuth, J.R. Gord, *Water-Vapor Detection Using Asynchronous THz Sampling*, Applied Spectroscopy **60**, 3 (2006).

[18] E.A. Shaner, *Picosecond Waveguide Spectroscopy and Time-Resolved Ballistic Electron Transport*, Ph.D. Dissertation, Princeton University, (2004).

[19] A. Rogalski, *Infrared Detectors* (Taylor and Francis CRC Press, Boca Raton, FL., 2000), p. 149.